Science Advances
AAAS

Supplementary Materials for

How does salinity shape ocean circulation and ice geometry on Enceladus and other icy satellites?

Wanying Kang *et al.*

Corresponding author: Wanying Kang, wanying@mit.edu

Sci. Adv. **8**, eabm4665 (2022)
DOI: 10.1126/sciadv.abm4665

This PDF file includes:

Exploring the sensitivity of ocean model solutions to parameters
Section S1
Figs. S1 to S11
References

1 Exploring the sensitivity of ocean model solutions to parameters

1.1 Sensitivity to heat partition between the core and the shell

To examine the sensitivity of ocean circulation to core-shell heat partition, we repeat the same set of simulations with 100% heat produced in the core. The equilibrium ocean solutions are presented in Fig.S1 for the core-heating scenarios. All experiments are run out to full equilibrium and so the bottom heat flux is transmitted upward to the water-ice interface without loss in an integral sense, but with ocean currents shaping regional contributions. Compared to our default calculation, the shell-heating scenario shown in Fig.3 of the main text, there is no qualitative change. This is to be expected because the dominant forcing of the flow is the salinity and heat exchange between ice and ocean: the vertical temperature gradient induced by bottom heating is much smaller than the temperature gradient at the water-ice interface induced by the pressure dependence of the freezing point of water. Bottom warming induces stronger stratification if the ocean is fresher than 22 psu (when $\alpha < 0$), and vice versa. As can be seen by comparing Fig.S1 with Fig.3, the strengthening/weakening of the stratification suppresses/enhances the vertical extent over which the overturning circulation reaches into the deep ocean. The change is most pronounced at low salinity (4 psu), because the negative thermal expansion coefficient in a fresh ocean suppresses the parameterized convection, resulting in bottom water warming up. However, even with a mean salinity of 4 psu, the response of the dynamics to these stratification changes is rather small (compare the left columns of Fig.3 and Fig.S1 here).

1.2 Sensitivity to assumed ice viscosity

The viscosity of the ice shell controls ice speeds (Eq. 24 in the main text), and thereby the freezing/melting rate needed to maintain the observed ice geometry. However, due to our limited understanding of ice rheology, the uncertainties associated with the melting point ice viscosity η_m remain. To examine sensitivity we carried out an experiment with η_m set to 2×10^{13} Pa·s, 5 times lower than the default value. Solutions for the highest and the lowest salinity scenarios and one intermediate salinity scenarios with the lowest $I_{\rm mis}$ are presented in Fig. S2. Decreasing the ice viscosity leads to a stronger salinity flux between the ocean and ice (Eq. 21 in the main text) and stronger salinity variations. This can be clearly seen by comparing Fig. S2b with Fig. 3b of the main text. Since the overall salinity gradient increases, the density gradient also increases (Fig. S2c), and this in turn drives stronger circulation (Fig. S2e). In addition to these change, increasing ice mobility lowers the transitional salinity as shown by plus sign symbols in Fig. 4e of the main text. That is because a more negative thermal expansion coefficient is required to cancel the salinity-induced density anomaly and achieve a minimum density gradient, indeed just as suggested by our conceptual model. The opposite is true with increased ice viscosity. Because the salinity flux between the ocean and ice decreases, the overall salinity gradient decreases, and that make cancellation between the temperature- and salinity-driven circulation occur at higher salinity (see minus sign symbols in Fig. 4e of the main text).

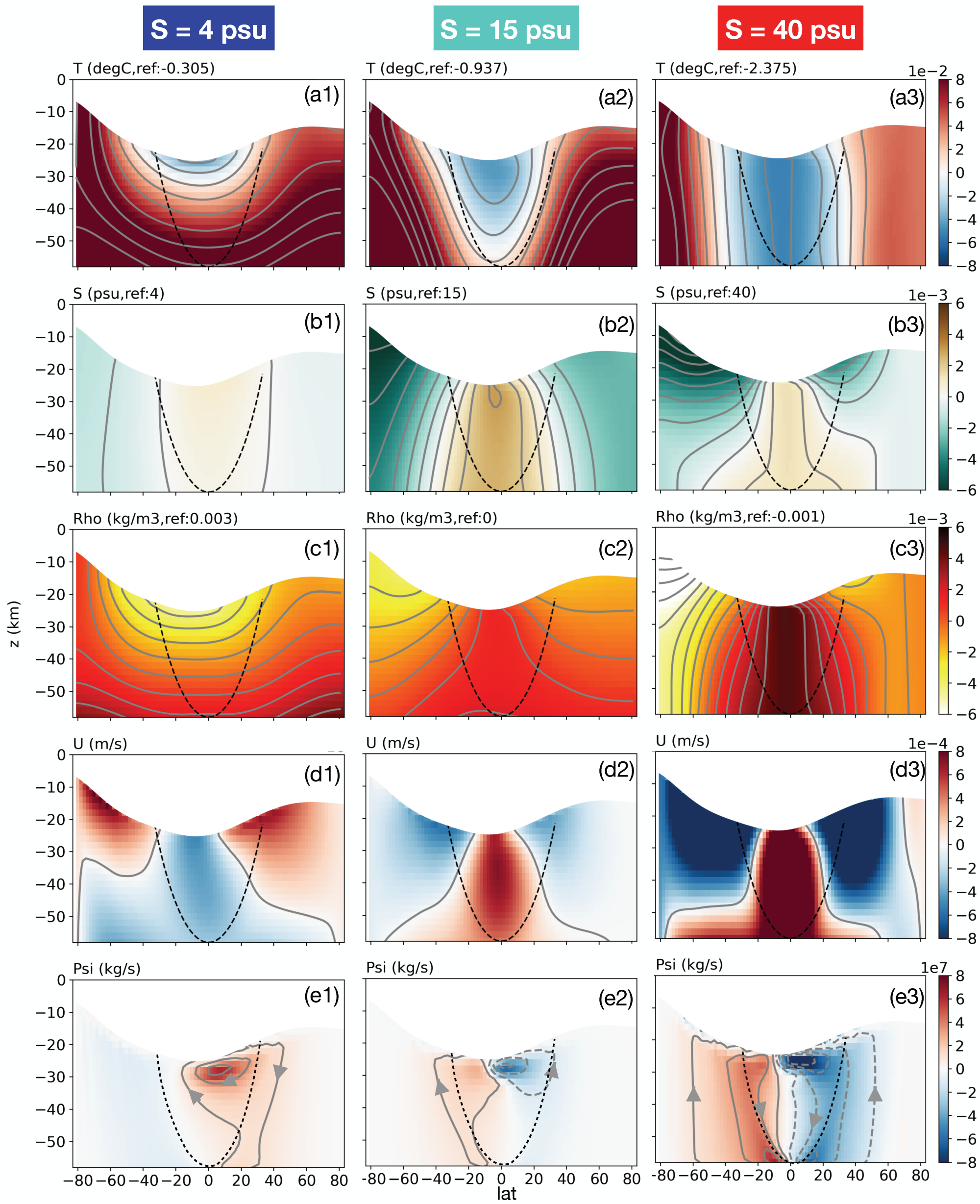

Figure S1: Solution for the core-heating scenario. Laid out the same way as Fig.3 of the main text. Default mixing parameters are used.

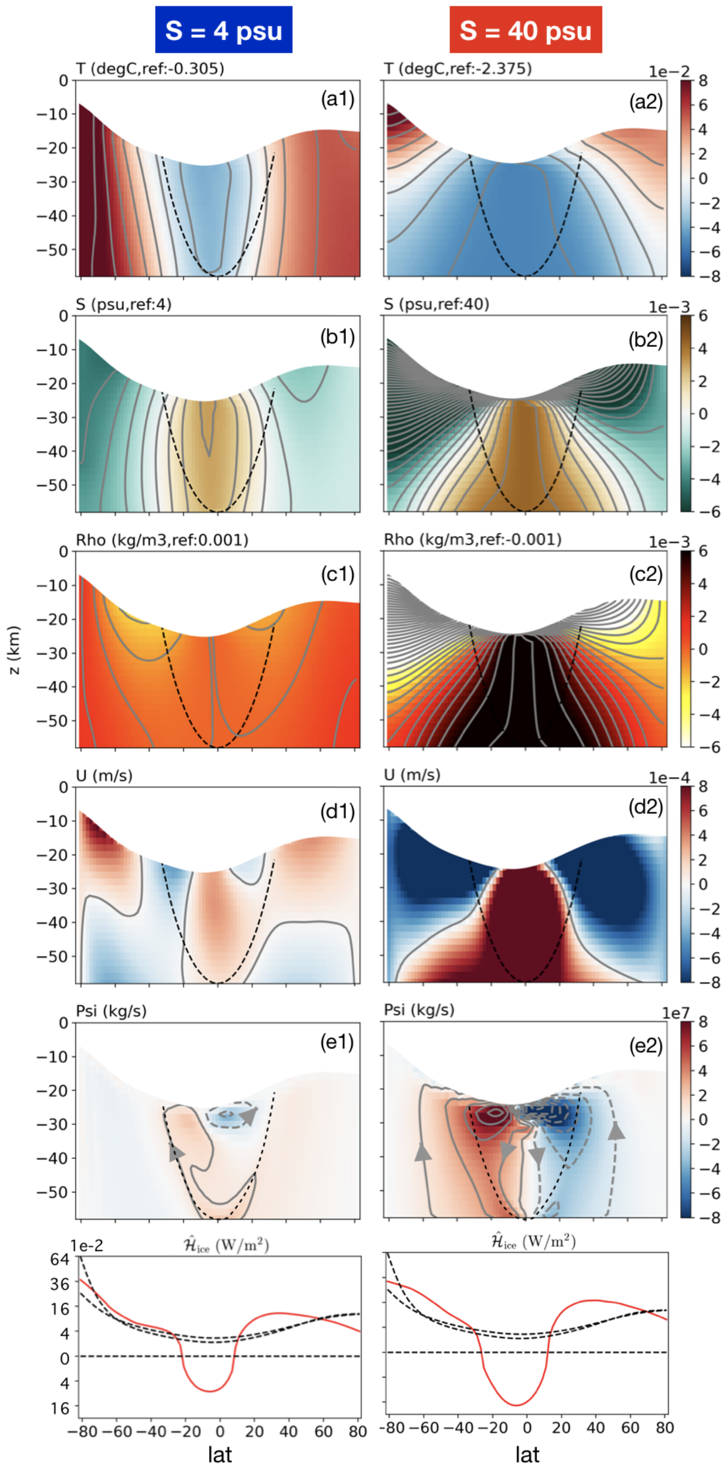

Figure S2: The sensitivity of the 100% shell-heating scenario solution to lower ice viscosity ($\eta_m = 2 \times 10^{13}$ Pa·s instead of 10^{14} Pa·s). Rows (a-e) are the set out the same as in Fig. S1. Row (f) is similar to Fig. 4(c,d) of the main text and shows the inferred tidal dissipation $\mathcal{H}_{\rm ice}$ (red solid line, calculated using Eq. 2 in the main text), compared with the dissipation rate predicted by our tidal dissipation model (black dashed lines, Eq.26 in the main text).

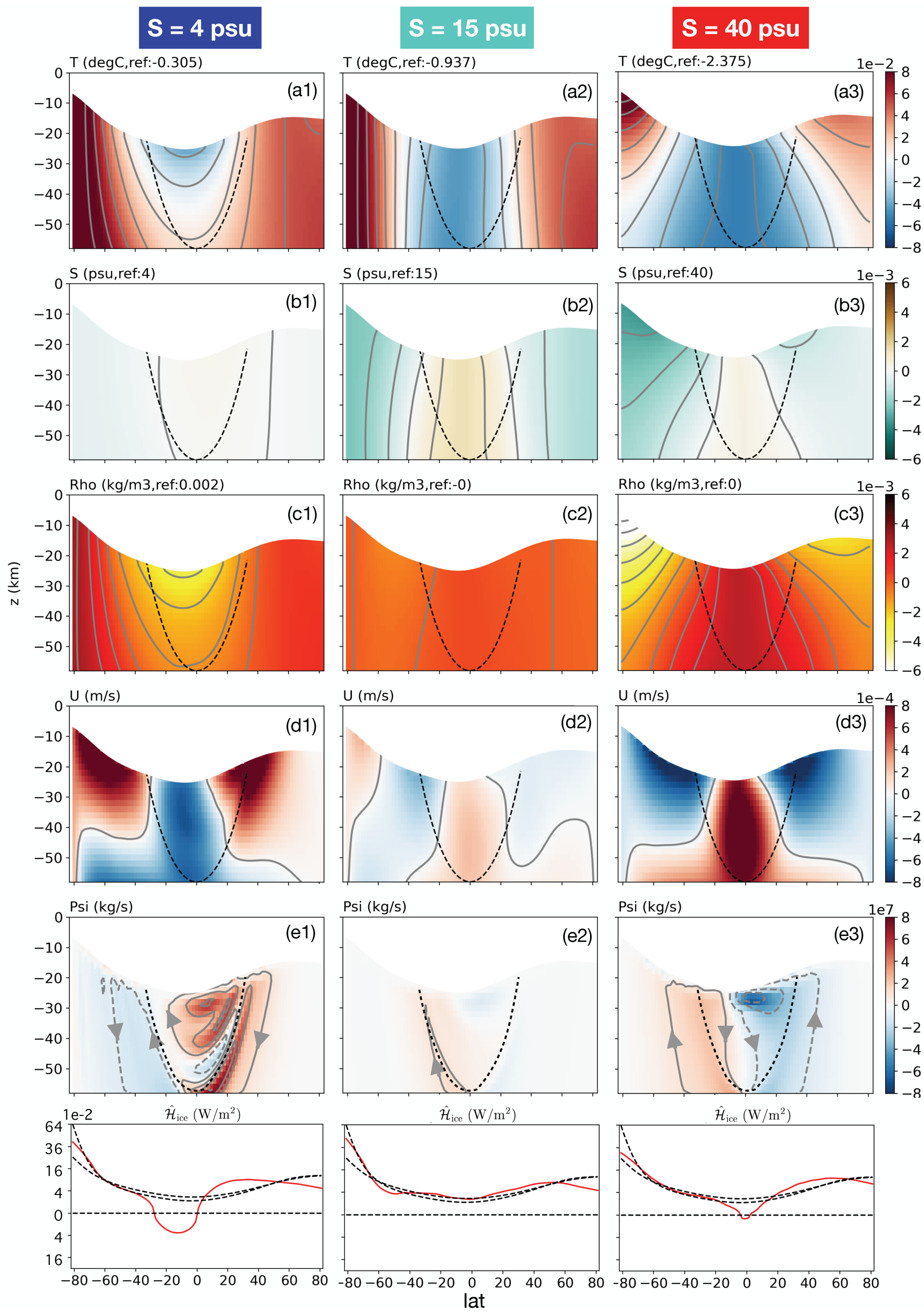

Figure S3: The sensitivity of the 100% shell-heating scenario solution to higher ice viscosity ($\eta_m = 5 \times 10^{14}$ Pa·s instead of 10^{14} Pa·s), set out as in Fig. S2.

1.3 Sensitivity to diffusivity and viscosity

To examine the sensitivity to diffusivity and viscosity, we carried out four additional sets of experiments for the shell-heating scenario using different mixing coefficients: one with 5 times high viscosity $\nu_h = \nu_v = 50$ m^2/s, one with 10 times lower viscosity $\nu_h = \nu_v = 1$ m^2/s, one with 5 times lower diffusivity $\kappa_h = \kappa_v = 0.001$ m^2/s, and in the last test, we turn on the Gent-McWilliams scheme (*49, 67*) to account for the mixing along the isopycnals induced by baroclinic eddies. The corresponding solutions for $S_0 = 4,\ 10$ and 40 psu are shown in Fig. S7, Fig. S8, Fig. S4 and Fig. S6, respectively. The mismatch index that measures the discrepancy between the inferred and predicted ice tidal dissipation (Eq. 3 in the main text) are plotted on Fig. 4e in the main text using triangular markers.

On changing GM and diapycnal diffusivities, the dependence of the meridional heat transport and hence the inferred tidal dissipation on salinity remains qualitatively similar to the control experiments: compare the bottom panels of Fig. S4-S9 with Fig. 4c in the main text. The mismatch between the inferred tidal dissipation $\hat{\mathcal{H}}_{\text{ice}}$ and the modeled dissipation $\mathcal{H}_{\text{ice}}$ is smallest when the reference salinity is in the range 10-20 psu regardless of the spread of diffusivities being used. The ocean solutions also remain qualitatively similar to the control experiments shown in Fig. 3 in the main text. Low salinity cases have sinking over the poles, driven in the main by the density gradient associated with temperature anomalies (see left panels of Fig. S4-S9). The opposite is true for the high salinity cases (see the right panels). At intermediate salinities ($\sim$10 psu), the density gradient and overturning circulation are weak (see the middle panels), just as in the control solutions (Fig. 3 in the main text). This weak circulation, in turn, leads to a weaker heat convergence toward the equator compared to the end-member cases (see bottom panels in Fig. S4-S9), and the resulting $\hat{\mathcal{H}}_{\text{ice}}$ is more consistent with $\mathcal{H}_{\text{ice}}$ (black dashed curves). This general trend is found in all diffusivity scenarios (Fig. 4e in the main text), suggesting that our main conclusions are robust.

There are quantitative changes to our solutions, however. With a lower κ_v, circulation tends to be confined in a shallower layer under the ice shell as a result of the incapability to mix the surface temperature and salinity anomalies downward (see Fig. S4), and this shallower circulation leads to weaker ocean heat transport and a lower $I_{\rm mis}$ overall. These changes are most pronounced in the 40 psu case probably because the ocean circulation cannot be efficiently energized when the buoyancy source is located higher in the water column than the buoyancy sink (*24*). However, when the vertical diffusivity is further reduced to 10^{-5} m^2/s, the heat transport near the equator strengthens significantly especially for S=40 psu (see bottom panels of Fig. S5), possibly cause by the strong temperature gradients developed underneath the ice shell in lack of vertical diffusion (see Fig. S5-a3). With GM on, the total (overturning plus GM parameterized) circulation and the heat transport enhance (see Fig. S6e,f), driving $I_{\rm mis}$ up, due to the contribution by parameterized eddies (see Fig.4e).

The assumed viscosity also affects our solutions. Higher viscosity increases the Ekman layer depth following $\sqrt{2\nu_v/f}$, allowing us to simulate it despite the coarse resolution employed. Shown in Fig. S7 are the solutions obtained with 5 times stronger viscosity. Under this configuration, a shallow boundary circulation form underneath the ice shell, and the interior flow no longer follow the direction of rotating axis as it should be in absence of momentum drag. Toward the opposite limit, reducing viscosity by a factor of 10 forces the interior meridional flow to be better aligned with the rotating axis as shown by Fig. S8e, and it also removes the zonal flow gradient along the axial direction as shown by Fig. S 8d. Without the upper boundary circulation, the heat transport efficiency decreases, but the change in $I_{\rm mis}$ is less significant than that induced by increasing viscosity. Also, as viscosity reduces, the flow profile and circulation pattern start to show abrupt transitions over short spatial scale – that naturally requests higher resolution to resolve. To verify the results, we repeat the low viscosity experiments using 4 times higher resolution for $S = 4,\ 10,\ 40$ psu, and the solutions are shown in

Fig. S9. There is no qualitative change compared to the low resolution simulations, except that the circulations are allowed to better follow the direction of the rotating axis. The heat transport becomes slightly more efficient, but the dependence on salinity remain unchanged.

1.4 3D dynamics

We also carried out sensitivity tests at higher spatial resolution assuming 3D rather than 2D dynamics. This allows us to explicitly resolve the baroclinic eddies and their impacts on heat transport, at least partially. Here, we use a 0.25 degree resolution to simulate a narrow longitudinal section of 10 degrees to keep the computational cost manageable. Smagorinsky scheme (*75*) is turned on to better resolve the different dynamics across different latitudes. Unlike the fixed viscosity scheme, Smagorinsky scheme chooses viscosity based on motions that are resolved. Following previous oceanographic studies, the Smagorinsky viscosity constant is set to 4 and the explicit viscosity is set to 0.001, which is far below what is assumed for 2D experiments. The rest of mixing coefficients are kept the same as the default 2D simulations. As shown in Fig. S10, the temperature, salinity, density, zonal flow and the overturning circulation remain qualitatively similar to the 2D experiments except that the tracer contour lines tend to have shallower slopes here due to the slantwise convection and along-isopycnal mixing induced by baroclinic eddies and that jets form in regions with strong baroclinic instability. To demonstrate the simulated eddies, we show the zonal anomalies of temperature, vertical speed and zonal speed in Fig.S11. For all scenarios considered here, the equatorial region is dominated by aligned "rolls" and the polar regions are dominated by plumy kind of structures. This is somewhat similar to previous works (*41, 76, 77*), despite that our simulations are not driven by bottom heating as in previous works, but by the meridional buoyancy gradient near the ice shell. The detail analysis of the eddy dynamics and transport is beyond the scope of this paper, and we leave that for future works.

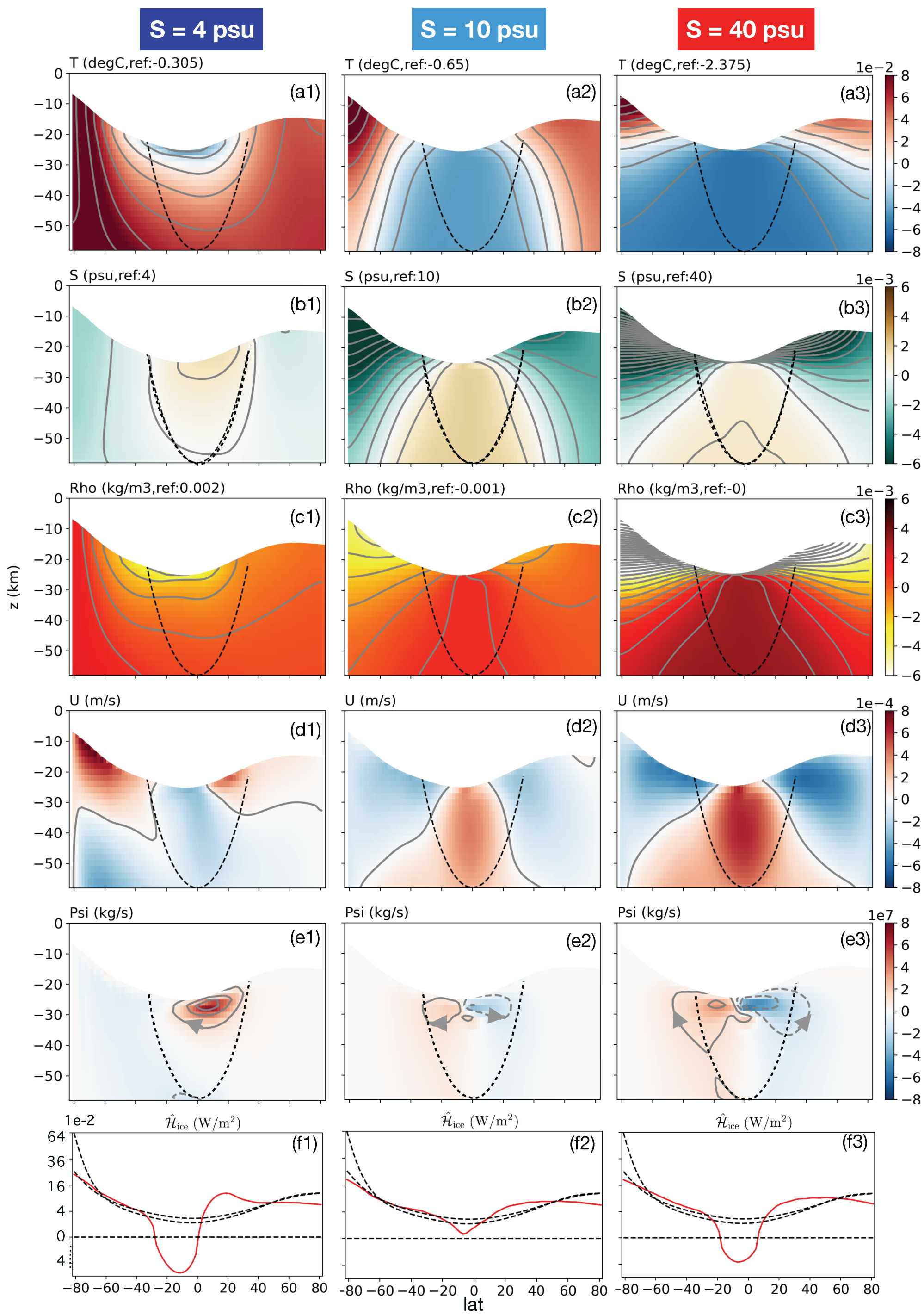

Figure S4: Sensitivity test to lower explicit diffusivity ($\kappa_v = \kappa_h = 10^{-3}$ m^2/s), set out as in Fig. S2.

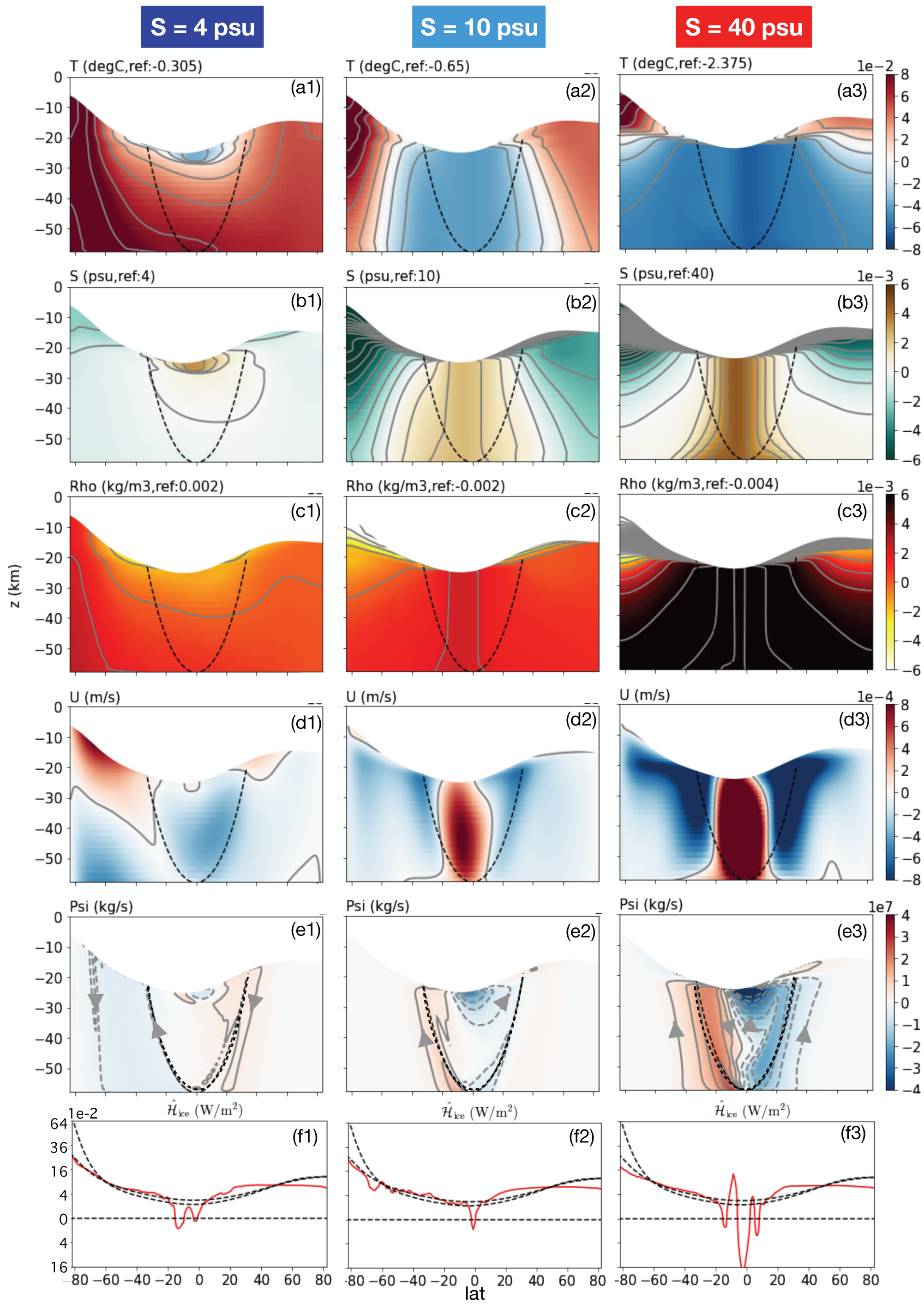

Figure S5: Sensitivity test to even lower diffusivity ($\kappa_v = 10^{-5}$ m^2/s and $\kappa_h = 10^{-3}$ m^2/s). To capture the strong gradients underneath the ice shell, we use 4 times higher resolution as in Fig.S9. Plots are laid out as in Fig. S2.

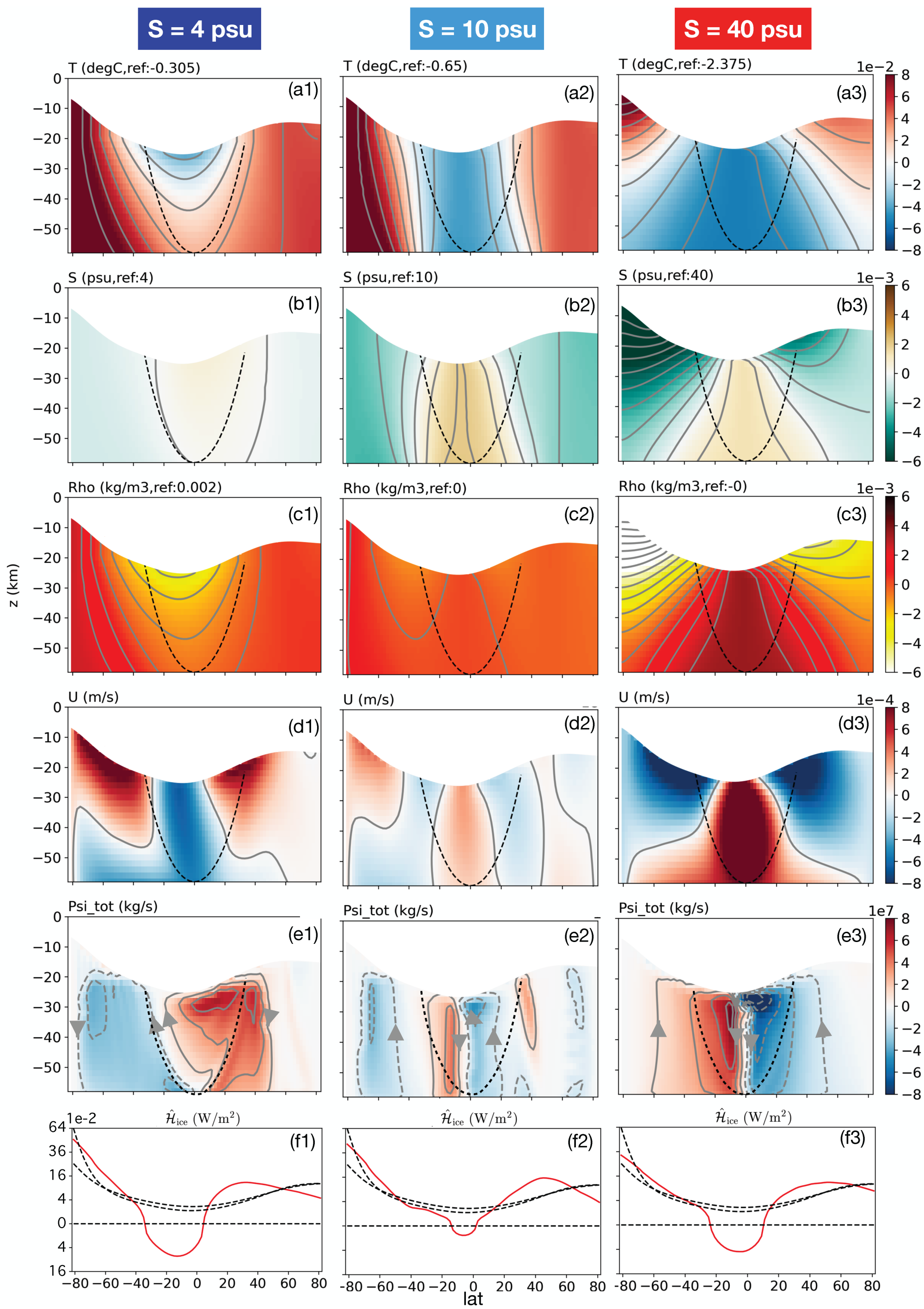

Figure S6: Sensitivity test to turning on Gent-McWilliams-Redi parameterization (*49, 67*), set out as in Fig. S2.

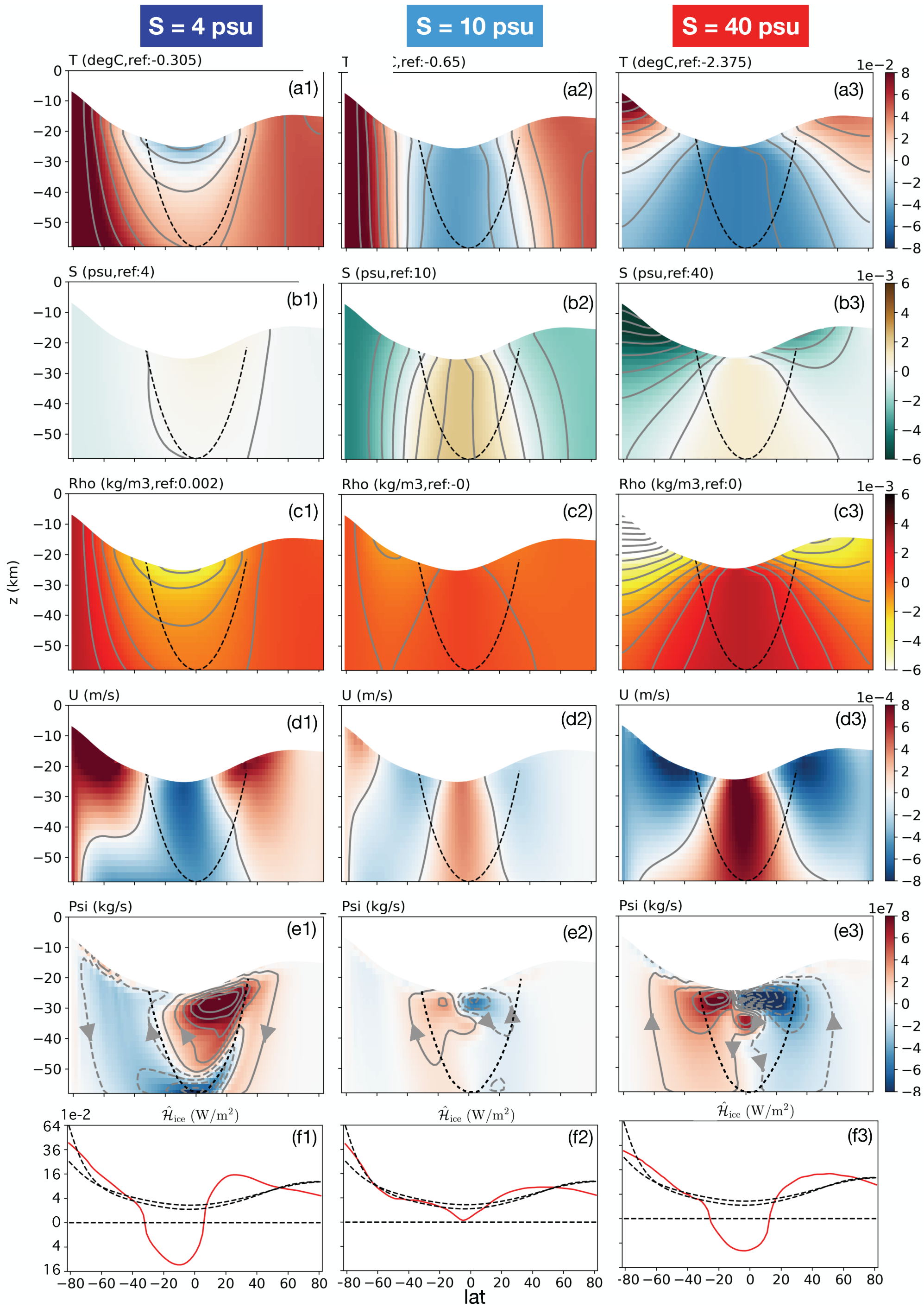

Figure S7: Sensitivity test to 5 times higher viscosity ($\nu_v = \nu_h = 50$ m^2/s instead of 10 m^2/s), set out as in Fig. S2.

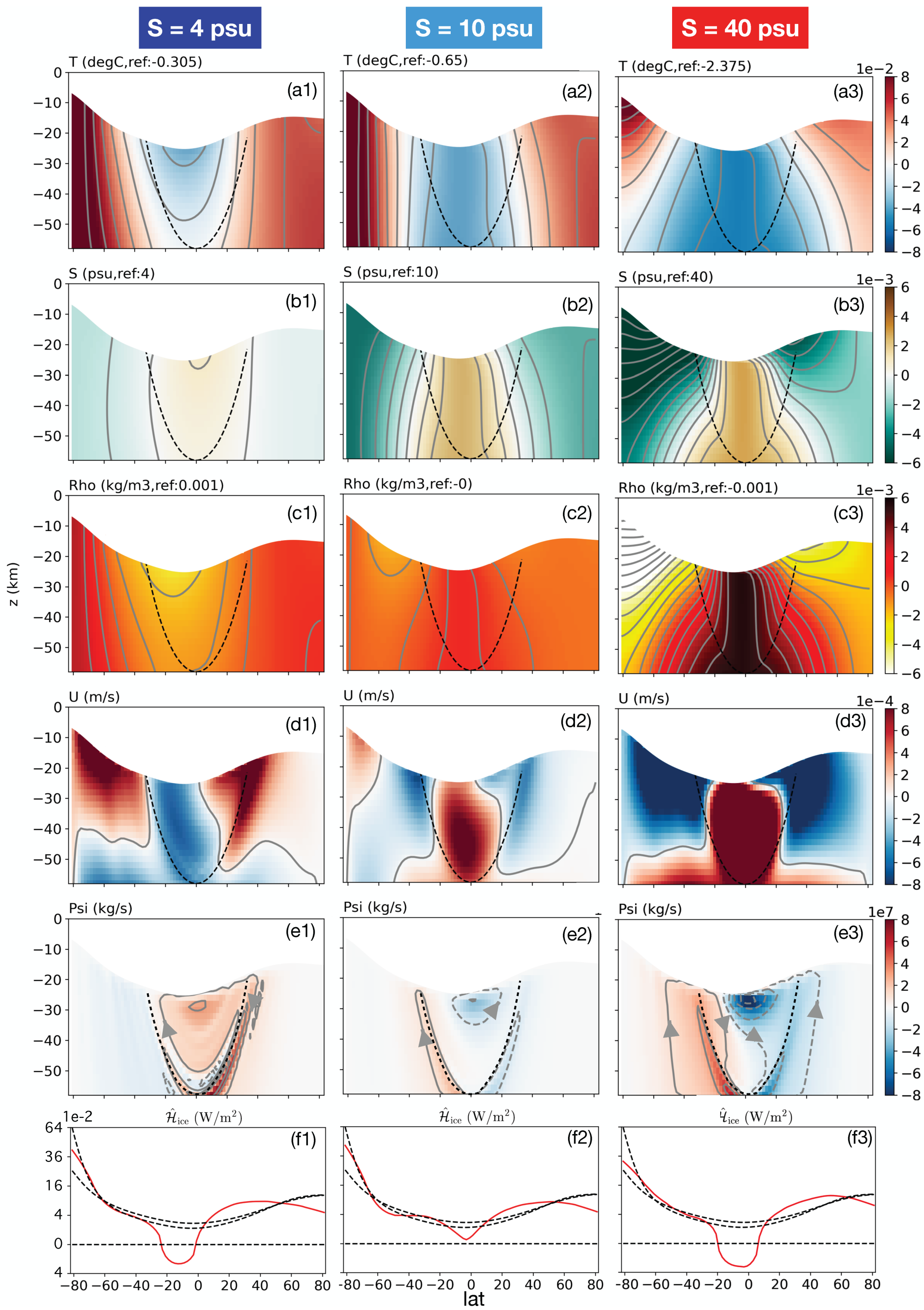

Figure S8: Sensitivity test to lower viscosity ($\nu_v = \nu_h = 1$ m^2/s instead of 10 m^2/s), set out as in Fig. S2.

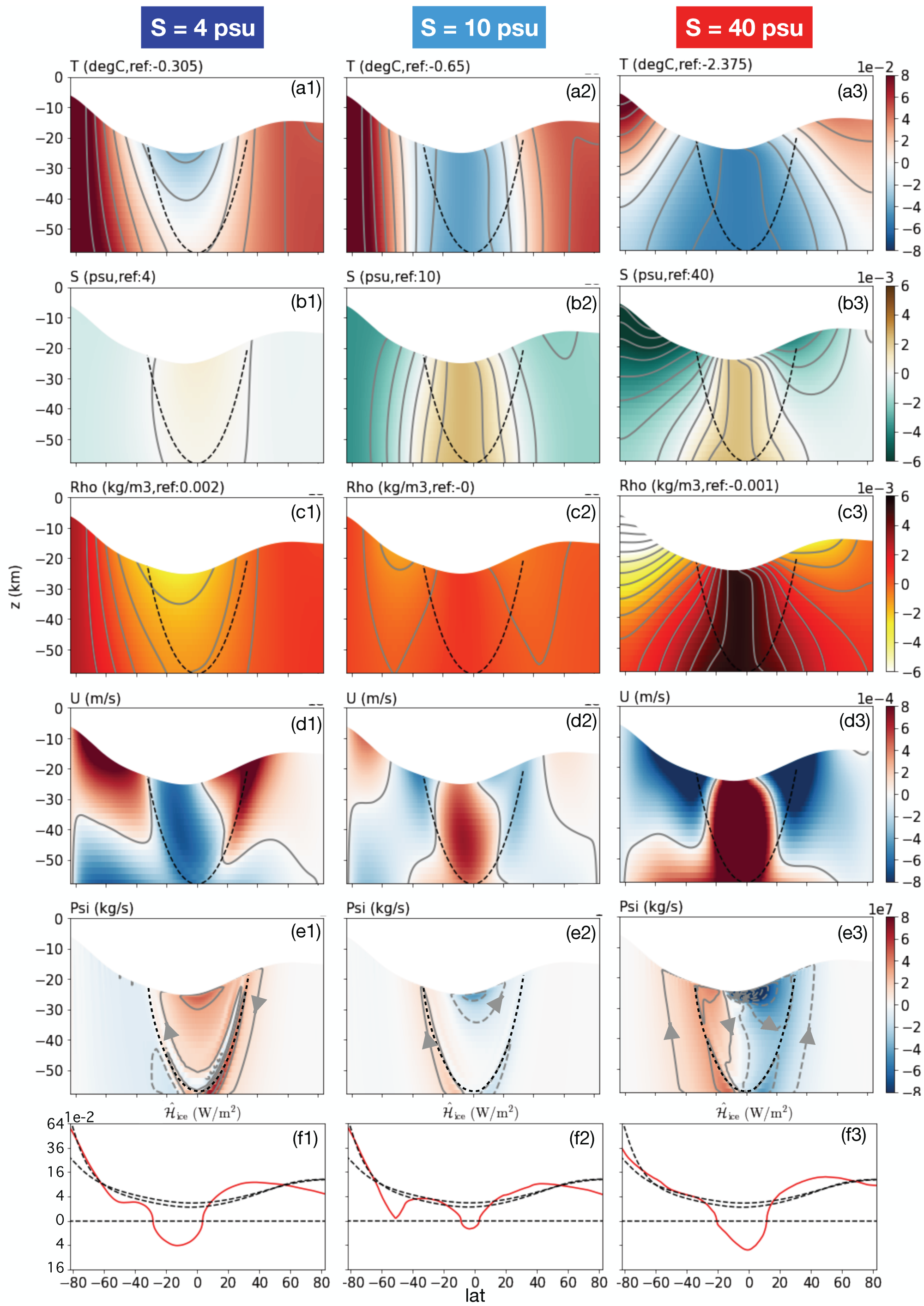

Figure S9: Repeating the same experiments as in Fig. S8 using 4 times higher resolution. Plots are set out as in Fig. S2.

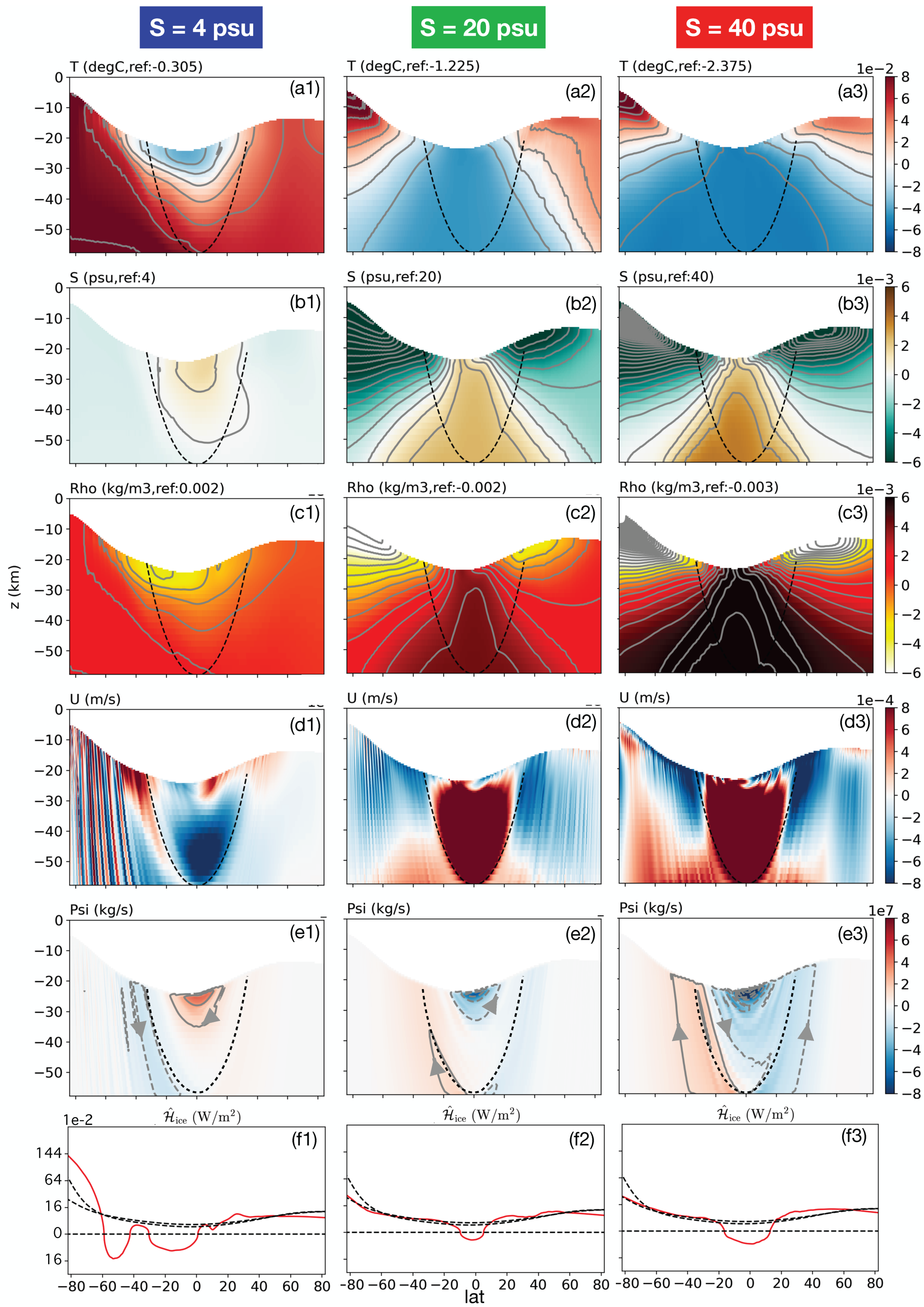

Figure S10: The sensitivity of the 100% shell-heating scenario solution to 3D dynamics at higher resolution (0.25 degree instead of 2 degree). Default parameters are used. What is shown is zonal mean values, and the plots are set out the same way as in Fig. S2.

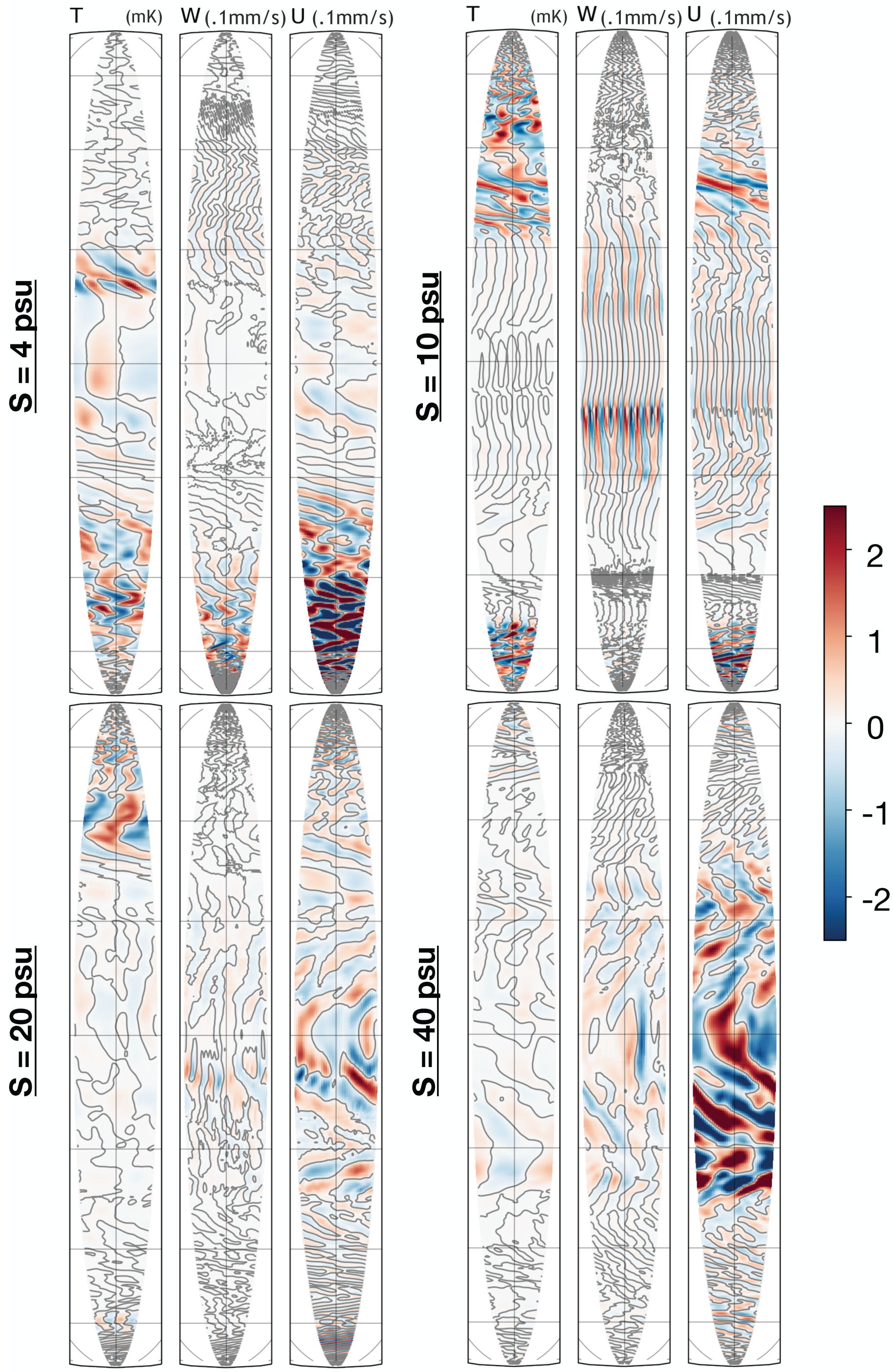

Figure S11: Eddy dynamics in 3D simulations. Within each panel, from left to right shown are the zonal anomalies of temperature, vertical speed and zonal speed. The four panels correspond to the four salinity scenarios as indicated by the titles. Zero contours are plotted on top of shadings.

REFERENCES

1. F. Postberg, S. Kempf, J. Schmidt, N. Brilliantov, A. Beinsen, B. Abel, U. Buck, R. Srama, Sodium salts in E-ring ice grains from an ocean below the surface of Enceladus. *Nature* **459**, 1098–1101 (2009).

2. P. C. Thomas, R. Tajeddine, M. S. Tiscareno, J. A. Burns, J. Joseph, T. J. Loredo, P. Helfenstein C. Porco, Enceladus's measured physical libration requires a global subsurface ocean. *Icarus* **264**, 37–47 (2016.

3. G. Choblet, G. Tobie, C. Sotin, M. Běhounková, O. Čadek, F. Postberg, O. Souček, Powering prolonged hydrothermal activity inside Enceladus. *Nat. Astron.* **1**, 841–847 (2017).

4. M. Beuthe, Enceladus's crust as a non-uniform thin shell: II tidal dissipation. *Icarus* **332**, 66–91 (2019).

5. J. H. Waite Jr., M. R. Combi, W.-H. Ip, T. E. Cravens, R. L. McNutt Jr., W. Kasprzak, R. Yelle, J. Luhmann, H. Niemann, D. Gell, B. Magee, G. Fletcher, J. Lunine, W.-L. Tseng, Cassini ion and neutral mass spectrometer: Enceladus plume composition and structure. *Science* **311**, 1419–1422 (2006).

6. H.-W. Hsu, F. Postberg, Y. Sekine, T. Shibuya, S. Kempf, M. Horányi, A. Juhász, N. Altobelli, K. Suzuki, Y. Masaki, T. Kuwatani, S. Tachibana, S.-I. Sirono, G. Moragas-Klostermeyer, R. Srama, Ongoing hydrothermal activities within Enceladus. *Nature* **519**, 207–210 (2015).

7. J. H. Waite, C. R. Glein, R. S. Perryman, B. D. Teolis, B. A. Magee, G. Miller, J. Grimes, M. E. Perry, K. E. Miller, A. Bouquet, J. I. Lunine, T. Brockwell, S. J. Bolton, Cassini finds molecular hydrogen in the Enceladus plume: Evidence for hydrothermal processes. *Science* **356**, 155–159(2017).

8. F. Postberg, N. Khawaja, B. Abel, G. Choblet, C. R. Glein, M. S. Gudipati, B. L. Henderson, H.-W. Hsu, S. Kempf, F. Klenner, G. Moragas-Klostermeyer, B. Magee, L. Nölle, M. Perry,

R. Reviol, J. Schmidt, R. Srama, F. Stolz, G. Tobie, M. Trieloff, J. H. Waite, Macromolecular organic compounds from the depths of Enceladus. *Nature* **558**, 564–568 (2018).

9. R.-S. Taubner, P. Pappenreiter, J. Zwicker, D. Smrzka, C. Pruckner, P. Kolar, S. Bernacchi, A. H. Seifert, A. Krajete, W. Bach, J. Peckmann, C. Paulik, M. G. Firneis, C. Schleper, S. K.-M. R. Rittmann, Biological methane production under putative Enceladus-like conditions. *Nat. Commun.* **9**, 748 (2018).

10. C. R. Glein, J. H. Waite, The carbonate geochemistry of Enceladus' ocean. *Geophys. Res. Lett.* **47**, e2019GL085885 (2020).

11. C. J. Hansen, L. Esposito, A.I.F. Stewart, J. Colwell, A. Hendrix, W. Pryor, D. Shemansky, R. West, Enceladus' water vapor plume. *Science* **311**, 1422–1425 (2006).

12. C. J. A. Howett, J. R. Spencer, J. Pearl, M. Segura, High heat flow from Enceladus' south polar region measured using 10–600 cm^{-1}Cassini/CIRS data. *J. Geophys. Res. Atmos.* **116**, 10.1029/2010JE003718 (2011).

13. J. R. Spencer, C. J. A. Howett, A. Verbiscer, T. A. Hurford, M. Segura and D. C. Spencer, *European Planetary Science Congress* **8**, EPSC2013 (2013).

14. L. Iess, D. J. Stevenson, M. Parisi, D. Hemingway, R. A. Jacobson, J. I. Lunine, F. Nimmo, J. W. Armstrong, S. W. Asmar, M. Ducci, P. Tortora, The gravity field and interior structure of Enceladus *Science* **344**, 78–80 (2014).

15. M. Beuthe, A. Rivoldini, A. Trinh, *Geophys. Res. Lett.* **43**, 10,088–10,096 (2016).

16. R. Tajeddine, K. M. Soderlund, P. C. Thomas, P. Helfenstein, M. M. Hedman, J. A. Burns, P. M. Schenk, True polar wander of Enceladus from topographic data. *Icarus* **295**, 46–60 (2017).

17. O. Čadek, O. Souček, M. Běhounková, G. Choblet, G. Tobie, J. Hron, Long-term stability of Enceladus' uneven ice shell. *Icarus* **319**, 476–484 (2019).

18. D. J. Hemingway, T. Mittal, Enceladus's ice shell structure as a window on internal heat production. *Icarus* **332**, 111–131 (2019).

19. C. McCarthy, R. F. Cooper, Tidal dissipation in creeping ice and the thermal evolution of Europa. *Earth & Planet. Sci. Lett.*. 185–194 (2016).

20. G. Tobie, A. Mocquet, C. Sotin, Tidal dissipation within large icy satellites: Applications to Europa and Titan. *Icarus* **177**, 534–549 (2005).

21. J. Rekier, A. Trinh, S. A. Triana, V. Dehant, Internal energy dissipation in Enceladus's subsurface ocean from tides and libration and the role of inertial waves. *J. Geophys. Res.* **124**, 2198–2212 (2019).

22. K. M. Soderlund, K. Kalousová, J. J. Buffo, C. R. Glein, J. C. Goodman, G. Mitri, G. Patterson, F. Postberg, M. Rovira-Navarro, T. Rüeckriemen, J. Saur, B.E. Schmidt, C. Sotin, T. Spohn, G. Tobie, T. Van Hoolst, S. D. Vance, B. Vermeersen, Ice-ocean exchange processes in the Jovian and Saturnian satellite.,*Space Sci. Rev.* **216**, 80 (2020).

23. T. J. McDougall, P. M. Barker, *SCOR/IAPSO WG* **127**, 1 (2011).

24. Y. Zeng, M. F. Jansen, Ocean circulation on Enceladus with a high- versus low-salinity ocean. *Planet. Sci. J.*, **2**, 151 (2021),.

25. J. Cullum, D. P. Stevens, M. M. Joshi, Importance of ocean salinity for climate and habitability. *Proc. Natl. Acad. Sci. U. S. A.* **113**, 4278–4283 (2016).

26. B. Cael, R. Ferrari, The ocean's saltiness and its overturning. *Geophys. Res. Lett.* **44**, 1886–1891 (2017).

27. B. J. Travis, G. Schubert, Keeping Enceladus warm. *Icarus* **250**, 32–42 (2015).

28. O. Souček, M. Běhounkova, O. Čadek, J. Hron, G. Tobie, G. Choblet, Tidal dissipation in Enceladus' uneven, fractured ice shell *Icarus* **328**, 218–231 (2019).

29. G. Robuchon, G. Choblet, G. Tobie, O. Čadek, C. Sotin, O. Grasset, Coupling of thermal evolution and despinning of early Iapetus. *Icarus* **207**, 959–971 (2010).

30. D. Shoji, H. Hussmann, K. Kurita, F. Sohl, Ice rheology and tidal heating of Enceladus. *Icarus* **226**, 10–19 (2013).

31. M. Běhounková, G. Tobie, G. Choblet, O. Čadek, Impact of tidal heating on the onset of convection in Enceladus's ice shell. *Icarus* **226**, 898–904 (2013).

32. Y. Gevorgyan, G. Boué, C. Ragazzo, L. S. Ruiz, A. C. Correia, Andrade rheology in time-domain. Application to Enceladus' dissipation of energy due to forced libration. *Icarus* **343**, 113610 (2019).

33. M. Y. Zolotov, An oceanic composition on early and today's Enceladus. *Geophys. Res. Lett.* **34**, 10.1029/2007GL031234 (2007).

34. M. Y. Zolotov, F. Postberg, *LPI* p. 2496 (2014).

35. C. R. Glein, F. Postberg, S. D. Vance, *Enceladus and the Icy Moons of Saturn* (University of Arizona Press, 2018) **39**.

36. A. P. Ingersoll, M. Nakajima, Controlled boiling on Enceladus. 2. Model of the liquid-filled cracks. *Icarus* **272**, 319–326 (2016).

37. M. G. Fox-Powell, C. R. Cousins, Partitioning of crystalline and amorphous phases during freezing of simulated enceladus ocean fluids. *JGR: Planets* **126**, e2020JE006628 (2021).

38. G. Tobie, G. Choblet, C. Sotin, *J. Geophys. Res - Atmospheres* **108**, 219 (2003).

39. A. C. Barr, A. P. Showman, *Europa* (Univ. Arizona Press, 2009), pp. 405–430.

40. Y. Ashkenazy, R. Sayag, E. Tziperman, Dynamics of the global meridional ice flow of Europa's icy shell. *Nat. Astron.* **2**, 49–43 (2018).

41. S. Bire, W. Kang, A. Ramadhan, J.-M. Campin, J. Marshall, Exploring ocean circulation on icy moons heated from below. *JGR: Planets* **127**, e2021JE007025 (2022).

42. A. H. Lobo, A. F. Thompson, S. D. Vance, S. Tharimena, A pole-to-equator ocean turning circulation on Enceladus. *Nat. Geosci.* 185–189 (2021).

43. M. Visbeck, J. Marshall, T. Haine, M. Spall, Specification of eddy transfer coefficients in coarse-resolution ocean circulation models*. *J. Phys. Oceanogr.* **27**, 381–402 (1997).

44. H. Jones, J. Marshall, Convection with rotation in a neutral ocean: A study of open-ocean deep convection *J. Phys. Oceanogr.* **23**, 1009 1039 (1993).

45. A. Czaja, J. Marshall, The partitioning of poleward heat transport between the atmosphere and ocean. *J. Atmos. Sci.* **63**, 1498–1511 (2006).

46. H. Jeffreys, On fluid motions produced by differences of temperature and humidity. *Quart. J. Roy. Meteor. Soc.* **51**, 347–356 (1925).

47. E. M. A. Chen, F. Nimmo, G. A. Glatzmaier, Tidal heating in icy satellite oceans. *Icarus* **229**, 11–30 (2014).

48. H. C. F. C. Hay, I. Matsuyama, Nonlinear tidal dissipation in the subsurface oceans of Enceladus and other icy satellites *Icarus* **319**, 68–85 (2019).

49. P. R. Gent, J. C. Mcwilliams, Isopycnal mixing in ocean circulation models. *J. Phys. Oceanogr.* **20**, 150–155 (1990).

50. W. Kang, G. Flierl, Spontaneous formation of geysers at only one pole on Enceladus's ice shell. *Proc. Natl. Acad. Sci. U.S.A.* **117**, 14764–14768 (2020).

51. H. Stommel, Thermohaline convection with two stable regimes of flow. *Tellus* **13**, 224–230 (1961).

52. J. Marshall, T. Radko, Residual-mean solutions for the Antarctic Circumpolar Current and its associated overturning circulation. *J. Phys. Oceanogr.* **33**, 2341–2354 (2003).

53. K. Hand, C. Chyba, Empirical constraints on the salinity of the europan ocean and implications for a thin ice shell. *Icarus* **189**, 424–438 (2007).

54. M. Y. Zolotov, E. L. Shock, Composition and stability of salts on the surface of Europa and their oceanic origin. *J. Geophys. Res. Planets* **106**, 32815–32827 (2001).

55. K. K. Khurana, M. G. Kivelson, K. P. Hand, C. T. Russell, in *Electromagnetic Induction from Europa's Ocean and the Deep Interior*, R. T. Pappalardo, W. B. Mc Kinnon, K. Khurana, Eds. (Europa, University of Arizona Press, 2009), pp. 572–586.

56. S. D. Vance, M. J. Styczinski, B. G. Bills, C. J. Cochrane, K. M. Soderlund, N. Gómez-Pérez, C. Paty, *J. Geophys. Res. Planets* **126**, e2020JE006418 (2021).

57. S. M. Howell, The likely thickness of Europa’s icy shell. *Planet. Sci.* **2**, 129 (2021).

58. F. Nimmo, P. Thomas, R. Pappalardo, W. Moore, The global shape of Europa: Constraints on lateral shell thickness variations. *Icarus* **191**, 183–192 (2007).

59. M. Zannoni, D. Hemingway, L. G. Casajus, P. Tortora, The gravity field and interior structure of Dione. *Icarus* **345**, 113713 (2020).

60. D. Durante, D. J. Hemingway, P. Racioppa, L. Iess, D. J. Stevenson, Titan's gravity field and interior structure after Cassini. *Icarus* **326**, 123–132 (2019).

61. F. Nimmo, B. G. Bills, Shell thickness variations and the long-wavelength topography of Titan. *Icarus* **208**, 896–904 (2010).

62. MITgcm-group, MITgcm User Manual, *Online documentation* (MIT/EAPS, 2010); http://mitgcm.org/public/r2_manual/latest/online_documents/manual.html.

63. J. Marshall, A. Adcroft, C. Hill, L. Perelman, C. Heisey, A finite-volume, incompressible Navier Stokes model for studies of the ocean on parallel computers. *J. Geophys. Res.* **102**, 5753–5766 (1997).

64. M. Losch, Modeling ice shelf cavities in a z-coordinate ocean general circulation model. *J. Geophys. Res.* **113**, 2007JC004368 (2008).

65. C. Wunsch, R. Ferrari, Vertical mixing, energy, and the general circulation of the oceans. *Ann. Rev. Fluid Mech.* **36**, 281–314 (2004).

66. B. A. Klinger, J. Marshall, U. Send, Representation of convective plumes by vertical adjustment. *J. Geophys. Res. Oceans* **101**, 18175–18182 (1996).

67. M. H. Redi, Oceanic isopycnal mixing by coordinate rotation. *J. Phys. Oceanogr.* **12**, 1154–1158 (1982).

68. T. J. McDougall, D. R. Jackett, D. G. Wright, R. Feistel, Accurate and computationally efficient algorithms for potential temperature and density of seawater. *J. Atmos. Oceanic Tech.* **20**, 730–741 (2003).

69. E. M. A. Chen, F. Nimmo, Obliquity tides do not significantly heat Enceladus, *Icarus* **214**, 779–781 (2011).

70. M. Beuthe, Crustal control of dissipative ocean tides in Enceladus and other icy moons. *Icarus* **280**, 278–299 (2016).

71. D. M. Holland, A. Jenkins, Modeling thermodynamic ice–ocean interactions at the base of an ice shelf. *J. Phys. Oceanogr.* **29**, 1787–1800 (1999).

72. J. P. Renaud, W. G. Henning, Increased tidal dissipation using advanced rheological models: implications for io and tidally active exoplanets. *ApJ* **857**, 98 (2018).

73. M. Beuthe, Enceladus's crust as a non-uniform thin shell: I tidal deformations. *Icarus* **302**, 145–174 (2018).

74. V. F. Petrenko, R. W. Whitworth, *Physics of Ice* (OUP Oxford, 1999).

75. J. Smagorinsky, General circulation experiments with the primitive equations. *Mon. Weath. Rev.* **91**, 99–164 (1963).

76. K. M. Soderlund, Ocean dynamics of outer solar system satellites. *Geophys. Res. Lett.* **46**, 8700–8710 (2019).

77. Y. Ashkenazy, E. Tziperman, Dynamic Europa ocean shows transient Taylor columns and convection driven by ice melting and salinity. *Nat. Commun.* **12**, 6376 (2021).